PHYSICAL REVIEW A **82**, 062502 (2010)

Molecular isotopic effects on coupled electronic and nuclear fluxes

A. Kenfack,[1] I. Barth,[1,2] F. Marquardt,[3,4] and B. Paulus[1]
[1] *Physikalische und Theoretische Chemie, Institut für Chemie und Biochemie, Freie Universität Berlin, D-14195 Berlin, Germany*
[2] *Max-Born-Institut, Max-Born-Strasse 2A, D-12489 Berlin, Germany*
[3] *Visualisierung und Datenanalyse, Zuse Institut Berlin, D-14195 Berlin, Germany*
[4] *Fachbereich Mathematik, Freie Universität Berlin, D-14195 Berlin, Germany*

(Received 1 October 2010; published 3 December 2010)

A full quantum treatment shows that coupled electronic and nuclear fluxes exhibit a strong sensitivity to a small mass change in a vibrating molecule. This has been exemplified with the existing isotopes of $H_2{}^+$ as well as few fictitious ones. We find that the fluxes undergo a significant change as one goes from one isotope of reduced mass μ to another. Other well-defined observables are likewise affected. It turns out that as a general rule, the heavier the isotope, the larger the flux, the smaller the dispersion, and the longer the revival period. While we were able to confirm analytically that the time at the first turning point scales as $\sqrt{\mu}$ and that the revival period changes linearly with μ, the mechanism of other observables remains subtle as the result of quantum interference highlighted by the pronounced difference observed on the dispersion pattern.

DOI: 10.1103/PhysRevA.82.062502 PACS number(s): 31.50.Bc, 82.20.Bc, 82.20.Wt

I. INTRODUCTION

Very recent advances in simultaneously tracking quantum electronic and nuclear fluxes in molecules are of great importance for the understanding of various physical and chemical processes [1–3]. Monitoring, for instance, these fluxes through a given dividing surface for a vibrating molecule or during a chemical reaction, the number of electrons and nuclei crossing the surface can be determined with high precision. Moreover, detailed information about the time scales as well as the directionality and the synchronicity of both electronic and nuclear fluxes constitutes another important issue.

Gauss's divergence theorem and the continuity equation are the main components of the method [1,2] used here, allowing expressions of fluxes in terms of the Born-Oppenheimer [4] electronic and nuclear densities. The excellent agreement obtained with the non–Born-Oppenheimer method [5] for the hydrogen molecular ion indicates that this method [1] should be considered as a promising candidate for large quantum systems. Similarly, the influence of initial conditions on quantum fluxes was explored soon after, showing, for instance, a completely different dispersion pattern depending on whether the process is initiated in the inner or in the outer region of the potential energy surface (PES) with respect to the equilibrium internuclear distance [2].

The isotope effect is one of the most studied phenomenon in chemical reactions as a small mass change can lead, in some situations, to a very dramatic response of the system. In the studies of collision processes, for example, it is shown that changing the reduced mass is equivalent to changing the potential, a fact that can be strongly manifested in the scattering lengths and in the cross sections [6–11]. A clear dependence on the isotope is also shown in many other issues, e.g., the solvation of molecules in water [12,13] or the molecular high harmonic generation [14]. Despite its great potential, the isotope effect on quantum fluxes has so far not been considered.

In this paper we analyze isotopes of hydrogen molecular ion $H_2{}^+$, and our objective is to demonstrate how small changes in the mass can alter the electronic and nuclear fluxes and related observables of the system. To allow for a more general trend, we artificially gradually vary the reduced mass from the muonium molecule $Mu_2{}^+$, through $H_2{}^+$, $D_2{}^+$, and $T_2{}^+$, until we reach a fictitious hydrogen molecular ion, whose mass is eight times larger than that of $H_2{}^+$. In this mass range, we have observed a change of several orders of magnitude on both the electronic and nuclear flux. Likewise, we show that related observables are also dramatically affected. The dependence of the time at the first turning point and the revival period on the reduced mass can be analytically explained with the help of the Morse oscillator model. Other observables like the dispersion happen to be very subtle and dominated by quantum effects.

The article is organized as follows. In Sec. II, we introduce our model and provide computational details of our observables. Section III shows the results of our numerical experiments with analytical evidence based on the Morse oscillator model. Section IV concludes the paper.

II. THE MODEL AND COMPUTATIONAL DETAILS

A. The model

The hydrogen molecular ion consists of one electron bound to two nuclei. The model that we briefly describe here governs each of its isotopes and has been extensively presented in [2]. We consider that the electron is described in cylindrical coordinates $(r\cos\phi, r\sin\phi, z)$ and assume that the nuclei are localized in the electronic z axis for the time scale we are interested in, which is shorter than the rotational time scale of the molecule. The nuclear motion is thus described by the internuclear distance R, parallel to z. Making use of the cylindrical symmetry imposed by these considerations, the electronic angular variable ϕ is eliminated, thereby leaving only three degrees of freedom (r,z,R) for the dynamics. The time-dependent Schrödinger equation (TDSE) for this three-body system has the following form (atomic units are used unless otherwise stated):

$$i\frac{\partial}{\partial t}\Psi(r,z,R,t) = \mathcal{H}\Psi(r,z,R,t), \qquad (1)$$

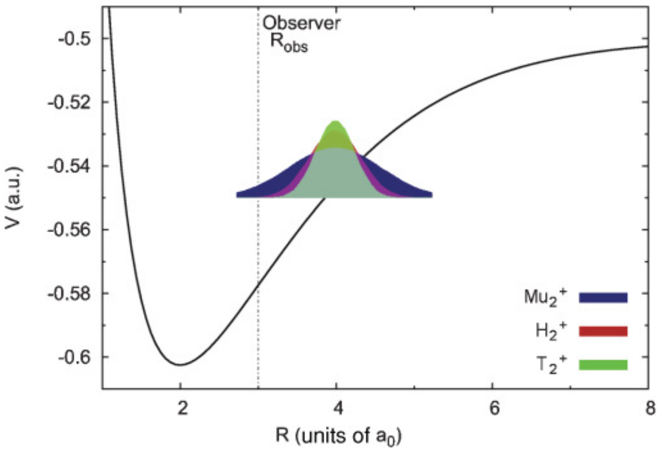

FIG. 1. (Color online) Initial nuclear wave packets of $\mathrm{Mu_2}^+$ (dark grey, blue online), $\mathrm{H_2}^+$ (medium grey, red online), and $\mathrm{T_2}^+$ (light grey, green online) placed on the electronic ground state $1s\sigma_g$. These wave packets are ground states of their respective neutral molecules, $\mathrm{Mu_2}$, $\mathrm{H_2}$, and $\mathrm{T_2}$, which have been promoted to the corresponding cationic ground state $1s\sigma_g$ at $R = R_0 = 4a_0$.

where $\Psi(r,z,R,t)$ is the total wave function of the electron and the nuclei and

$$\mathcal{H} = T_e + T_n + V_{nn} + V_{en}$$

is the molecular Hamiltonian in which $T_n = -1/(2\mu_n)\partial^2/\partial R^2$ is the kinetic energy of the nuclei with the reduced mass μ_n, $V_{nn} = 1/R$ is the nuclei-nuclei interaction,

$$T_e = -\frac{1}{2\mu_e}\frac{\partial^2}{\partial z^2} - \frac{1}{2\mu_e}\left(\frac{\partial^2}{\partial r^2} + \frac{1}{r}\frac{\partial}{\partial r}\right)$$

is the electronic kinetic energy with $1/\mu_e = 1 + 1/(4\mu_n)$, and

$$V_{en} = -\frac{1}{\sqrt{r^2 + (z - R/2)^2}} - \frac{1}{\sqrt{r^2 + (z + R/2)^2}}$$

is the electron-nuclei interaction. The initial state of this system is the Born-Oppenheimer (BO) wave function:

$$\Psi(r,z,R,t = 0) = \Psi_n(R,t = 0)\Psi_e(r,z;R). \qquad (2)$$

The nuclear wave function $\Psi_n(R,0)$ is the ground state of the neutral molecule $\mathrm{H_2}$ promoted to $\mathrm{H_2}^+$ at a given R_0. The electronic wave function $\Psi_e(r,z;R)$ is the $1s\sigma_g$ electronic ground-state wave function of $\mathrm{H_2}^+$ parameterized by the internuclear distance R. Figure 1 shows the potential energy surface $V(R)$ of the isotopes in the electronic ground state as well as some initial wave packets, namely, $\mathrm{Mu_2}^+$, $\mathrm{H_2}^+$, and $\mathrm{T_2}^+$, all centered at the internuclear distance $R_0 = 4a_0$. Note that although all these states possess the same energy, their widths are different: the smaller the reduced mass is, the larger the widths are, as one can clearly see from Fig. 1.

B. Computational details

The observables explored here are based upon the solution of the TDSE (1). The agreement between the exact method [15,16] and the BO approximation [1,2] was excellent. The use of the latter is computationally much faster and therefore also suitable for larger molecules in the future. To allow for a better understanding of our numerical experiments, we provide a few analytical expressions. The total wave function $\Psi(r,z,R,t)$ is approximated by the BO wave function $\Psi_{\mathrm{BO}}(r,z,R,t) = \Psi_n(R,t)\Psi_e(r,z;R)$, which is the product of the nuclear wave function $\Psi_n(R,t)$ and the electronic one $\Psi_e(r,z;R)$. Solving the following time-independent electronic Schrödinger equation,

$$\mathcal{H}_e\Psi_e(r,z;R) = V(R)\Psi_e(r,z;R), \qquad (3)$$

with $\mathcal{H}_e = T_e + V_{nn} + V_{en}$, one obtains both the PES $V(R)$ and the electronic wave function $\Psi_e(r,z;R)$. This equation is solved using the GAUSSIAN03 package [17] that involves a correlation-consistent polarized basis set (aug-cc-pV5Z) [18]. The computations are performed within the cylinder of radius $r_0 = 18.0a_0$ and height $2z_0 = 36.0a_0$ ($z \in [-z_0,z_0]$) with 50 and 110 grids, respectively; the nuclear degree of freedom $R \in [0.0,16.0a_0]$ is discretized with 256 grid points. We showed in [2] that with the above settings, a sufficiently high numerical accuracy is reached.

The PES is subsequently employed for the computation of the nuclear wave function $\Psi_n(R,t)$ by solving the time-dependent Schrödinger equation

$$i\frac{\partial}{\partial t}\Psi_n(R,t) = [T_n + V(R)]\,\Psi_n(R,t), \qquad (4)$$

using the symmetrized splitting method together with the fast Fourier transform [19,20]. Moreover, to avoid unphysical reflections at the boundary, an absorbing mask [21] for $R = 16.0a_0$ has been used.

From the total wave function $\Psi(r,z,R,t) \approx \Psi_{\mathrm{BO}}(r,z,R,t)$ the full density $\rho_{\mathrm{tot}}(r,z,R,t) = |\Psi(r,z,R,t)|^2$ is determined. The continuity equation reads

$$\dot{\rho}_{\mathrm{tot}}(r,z,R,t) = -\nabla\cdot\mathbf{j}(r,z,R,t), \qquad (5)$$

where $\mathbf{j} = (\mathrm{Im}(\Psi^*\nabla_e\Psi)/\mu_e, \mathrm{Im}(\Psi^*\nabla_n\Psi)/\mu_n)$ is the total current density containing the electronic ∇_e and nuclear ∇_n gradients. Integrating Eq. (5) over the nuclear degree of freedom, one obtains the reduced electronic continuity equation

$$\dot{\rho}_e(r,z,t) = -\nabla_e\cdot\mathbf{j}_e(r,z,t), \qquad (6)$$

and integrating over the electronic degrees of freedom, one obtains the reduced nuclear continuity equation

$$\dot{\rho}_n(R,t) = -\nabla_n\cdot\mathbf{j}_n(R,t), \qquad (7)$$

where ρ_e is the electronic density, ρ_n is the nuclear density, $\mathbf{j}_e$ is the electronic current density, and $\mathbf{j}_n$ is the nuclear current density.

The electronic and nuclear fluxes we are interested in are monitored through the observer surface A_{obs}, which is the boundary of the observer volume V_{obs}. The electronic flux F_e and the nuclear flux F_n defined as surface integrals are transformed in terms of the volume integrals by virtue of Gauss's divergence theorem as

$$F_e(t;A_{\mathrm{obs}}) = -\int_{A_{\mathrm{obs}}} d\mathbf{A}\cdot\mathbf{j}_e = \frac{d}{dt}\int_{V_{\mathrm{obs}}} dV\rho_e, \qquad (8)$$

$$F_n(t;A_{\mathrm{obs}}) = -\int_{A_{\mathrm{obs}}} d\mathbf{A}\cdot\mathbf{j}_n = \frac{d}{dt}\int_{V_{\mathrm{obs}}} dV\rho_n. \qquad (9)$$

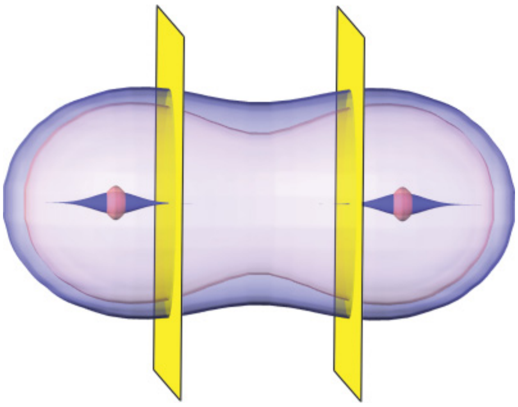

FIG. 2. (Color online) Visualization of the initial electronic and nuclear densities of $\mathrm{Mu_2}^+$ (black, blue online) and that of $\mathrm{T_2}^+$ (grey, red online). The electronic densities surround the nuclear ones. One clearly sees the difference between both densities, which is much more pronounced for nuclei. The two rectangular planes (grey, yellow online) are located at $z_{\mathrm{obs}} = \pm R_{\mathrm{obs}}/2$, where R_{obs} is the distance separating the two planes. This visualization has been created using the academic system ZIBAMIRA, a superset of its commercial version AMIRA [22].

Integrating Eqs. (8) and (9) over the time interval $[0,t]$, one obtains the corresponding electronic yield Y_e and the nuclear yield Y_n, given by

$$Y_e(t; A_{\mathrm{obs}}) = \int_0^t d\tau\, F_e(\tau; A_{\mathrm{obs}}), \tag{10}$$

$$Y_n(t; A_{\mathrm{obs}}) = \int_0^t d\tau\, F_n(\tau; A_{\mathrm{obs}}). \tag{11}$$

More specifically, the observer surface A_{obs} in our model is defined by two planes parallel to the plane $z = 0$ located at the internuclear separation distance R_{obs} for which the corresponding electronic observer coordinate is $z_{\mathrm{obs}} = \pm R_{\mathrm{obs}}/2$; see Fig. 2. This figure displays the visualization of the initial electronic and nuclear densities of $\mathrm{Mu_2}^+$ (black, blue online) together with that of $\mathrm{T_2}^+$ (grey, red online). The difference between the densities of the two entities is clearly noticeable and is very much pronounced for the nuclei. Exploring throughout our mass range, we confirmed the intuition as to which localization of the density is much stronger for larger masses.

III. RESULTS AND DISCUSSION

In this section we present and discuss our results as a function of time for each of the isotopes and as a function of the isotope mass. The isotopes of the hydrogen molecular ion $\mathrm{H_2}^+$ that we consider range from the muonium molecular ion $\mathrm{Mu_2}^+$ to the fictitious molecular ion $\mathrm{X_2}^+$ with eight times the reduced mass of $\mathrm{H_2}^+$. In addition to the coupled electronic and nuclear fluxes and yields, we have computed the electronic and nuclear dispersions, the observables related to the synchronicity and directionality of the fluxes, the mean bond length, and the autocorrelation functions.

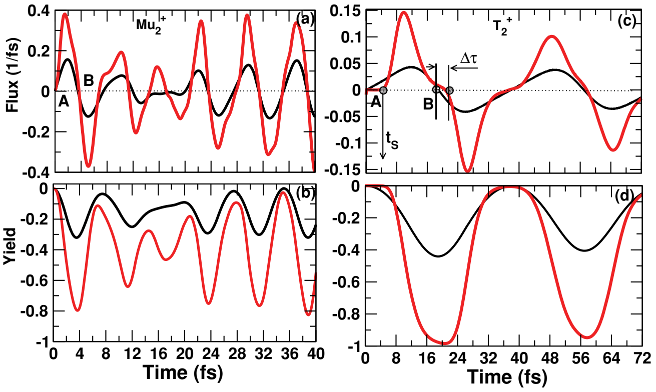

FIG. 3. (Color online) (a and c) Nuclear (grey, red online) and electronic (black) fluxes with (b and d) associated yields corresponding to $\mathrm{Mu_2}^+$ and $\mathrm{T_2}^+$, respectively. Here t_S is the time for which the nuclei start crossing the observer surface (region A), and $\Delta\tau$ is the time delay that the nuclei take to follow the electron when it first changes direction (region B).

A. The nuclear and electronic fluxes

Using Eqs. (8)–(11), we have computed nuclear and electronic fluxes as well as corresponding nuclear and electronic yields. Depicted in Fig. 3 are representative muonium $\mathrm{Mu_2}^+$ and tritium $\mathrm{T_2}^+$ cases. The curves in black are the electronic fluxes and yields, and those in grey (red online) are the nuclear ones. The oscillation frequency is far larger for $\mathrm{Mu_2}^+$ than $\mathrm{T_2}^+$, thus scaling with $1/\sqrt{\mu}$, as we will show later in this section. The magnitudes of both nuclear and electronic fluxes decrease as the reduced mass becomes larger; see Figs. 3(a) and 3(c). The heavier nuclei are likely to pass almost completely through the observer surface from the initial location to the opposite turning point and back, as can be seen from Figs. 3(b) and 3(d). Though more electronic yield passes through the observer surface for heavier isotopes, their maximum remains less than half of the electron that one would expect traveling with a nucleus that completely crosses the observer surface.

B. The starting nuclear flux time t_S and the time delay $\Delta\tau$

Analyzing in detail the question of synchronicity and directionality of nuclear and electronic fluxes, we have identified within the first oscillation period two regions, denoted by A and B, as shown in Figs. 3(a) and 3(c). The electron immediately flows through the observer surface as soon as the dynamics starts, in contrast to the nuclei that are delayed by the time t_S, which we call *starting nuclear flux time* t_S, recorded when the nuclear flux reaches 0.001 fs^{-1} (region A). This is because the electron density is much broader than the nuclei one and the dividing surface is not close to the initial location of the nuclear wave packet. Another quantity of interest is the time delay $\Delta\tau$ (region B) that nuclei take to follow the electron as it first changes direction at the observer surface. One can clearly see that the electron counterintuitively follows the nuclei (region B). These features highlighted by t_S and $\Delta\tau$ are caused by kinematic effects and strongly depend on the placement of the dividing surface. Figures 4 and 5 depict t_S and $\Delta\tau$ (squares) as a function of μ (the isotope reduced mass per reduced mass of $\mathrm{H_2}^+$), respectively. These quantities follow the power-law

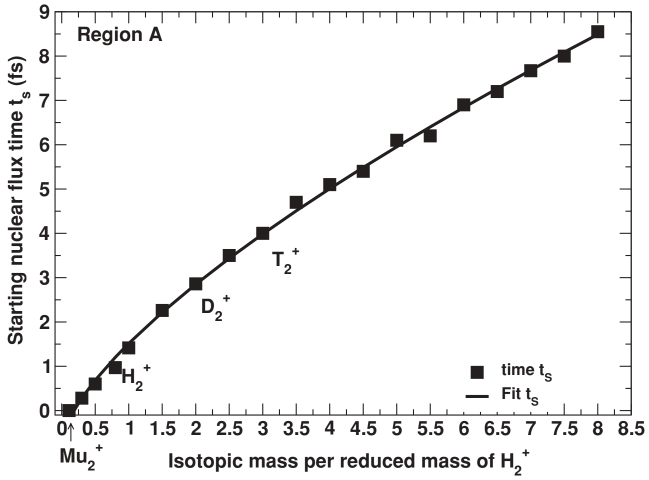

FIG. 4. Starting nuclear flux time t_S (squares), region A of Fig. 3, as a function of μ, the isotope reduced mass per reduced mass of $H_2{}^+$. Its corresponding fit (solid line) is $t_S = 2.18\mu^{0.7} - 0.66$.

fit (solid line) with $t_S = 2.18\mu^{0.7} - 0.66$ and $\Delta\tau = 0.70\mu^{0.84}$. This strictly nonlinear behavior may be attributed not only to the difference in the dispersion pattern observed in the subsequent section but also to the location of the diving surface.

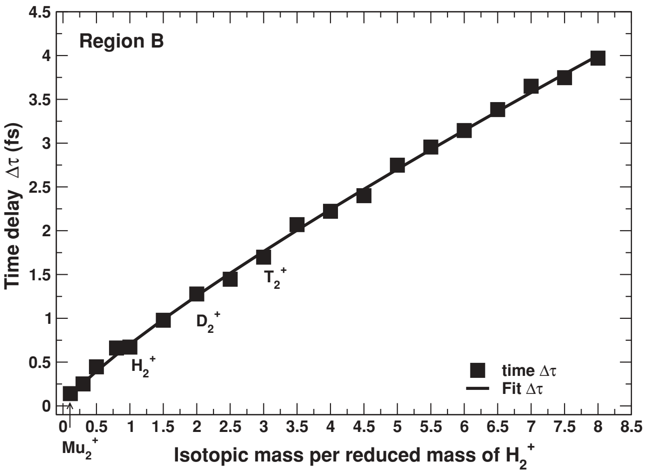

FIG. 5. Time delay $\Delta\tau$ (squares) that the nuclei take to follow the electron when it first changes direction at the observer surface (region B), as a function of the mass μ, the isotope reduced mass per reduced mass of $H_2{}^+$. Its corresponding fit (solid line) is $\Delta\tau = 0.70\mu^{0.84}$.

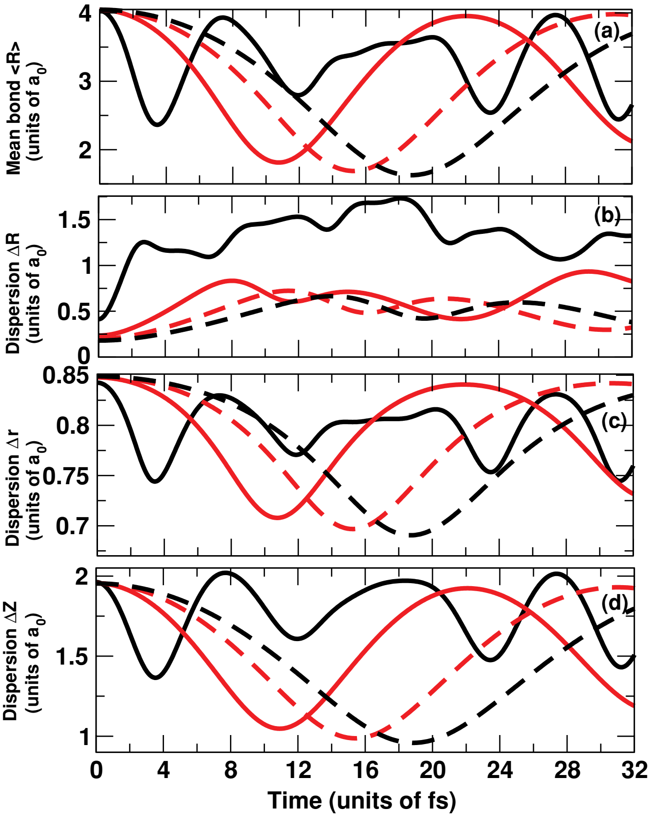

FIG. 6. (Color online) (a) Mean bond length, (b) nuclear dispersion ΔR, (c) electronic dispersion Δr, and (d) Δz for $Mu_2{}^+$ (solid black line), $H_2{}^+$ (solid grey line, red online), $D_2{}^+$ (dashed grey line, red online), and $T_2{}^+$ (dashed black line), as a function of time.

C. The nuclear and electronic dispersions

We have shown in [2] that the dispersion depends strongly on the initial location of the nuclear wave packet and that the nuclear dispersion, which, in general, is small as compared to the electronic one, may become increasingly high and eventually equal the electronic one if the dynamics starts at the inner region with respect to the equilibrium. Here the location of our initial wave packets is in the outer region, as shown in Fig. 1. We want to analyze the influence of the mass on these dispersions. In Fig. 6(a) we have plotted the mean bond length $\langle R\rangle$,

$$\langle R\rangle = \langle\Psi(r,z,R,t)|R|\Psi(r,z,R,t)\rangle; \tag{12}$$

we have also plotted the nuclear dispersion $\Delta R(t)$ [Fig. 6(b)], the electronic dispersion $\Delta r(t)$ [Fig. 6(c)], and $\Delta z(t)$ [Fig. 6(d)],

$$\Delta R(t) = \left(\int dR\,\rho_n(R,t)\,(R - \langle R\rangle)^2\right)^{1/2}, \tag{13}$$

$$\Delta r(t) = \left(\int r dr\,dz\,\rho_e(r,z,t)\,(r - \langle r\rangle)^2\right)^{1/2}, \tag{14}$$

$$\Delta z(t) = \left(\int r dr\,dz\,\rho_e(r,z,t)\,(z - \langle z\rangle)^2\right)^{1/2}, \tag{15}$$

as a function of time for some representative isotopes, namely, $Mu_2{}^+$, $H_2{}^+$, $D_2{}^+$, and $T_2{}^+$. The behavior of the mean bond is consistent with that observed in Sec. III A (Fig. 3). Clearly, its oscillation frequency decreases as the reduced mass increases. Moreover, the heaviest isotope is likely to come very close to the steepest wall at the inner turning point, as demonstrated in Fig. 7 with the minimum mean bond length $\langle R\rangle_{\min}$ (diamonds), whose nonlinear fit scales as $\mu^{-0.25}$ (solid line). It turns out that for any given isotope, the electronic dispersion is, in general, higher than the nuclear one. These results generalize what

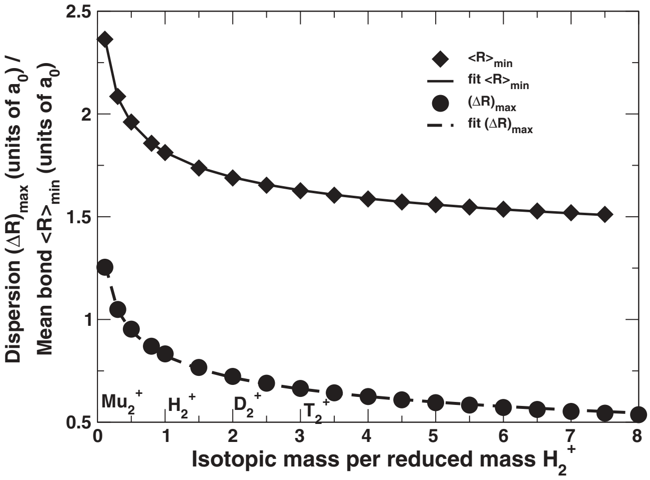

FIG. 7. Minimum mean bonds $\langle R\rangle_{\min}$ (diamonds), fit with $0.8/\mu^{0.25}+1.02$ (solid line), and maximum nuclear dispersion $(\Delta R)_{\max}$ (circles), fit with $0.82/\mu^{0.2}$ (dashed line), as a function of the mass μ of different isotopes per reduced mass of $H_2{}^+$. These data are recorded within each isotope oscillation period (see Fig. 6).

was already demonstrated for the deuterium molecular ion $D_2{}^+$ [2]. However, when restricted to the nuclear dispersions only, one remarkably notices that $Mu_2{}^+$ stands out, with its dispersion significantly higher than others. This nuclear dispersion increases as the isotope mass becomes smaller, thereby becoming larger than the electronic dispersion in r and eventually catching the electronic dispersion in z. As shown in Fig. 7, within the first oscillation periods the maximum nuclear dispersion $(\Delta R)_{\max}$ (circles) consequently decreases as the isotope mass increases, with a power-law behavior fit of $0.82/\mu^{0.2}$ (dashed line). The strong dispersion observed in Fig. 7 is consistent with the most probable quantum effect, namely, the underlined quantum interference, which is enhanced for light isotopes. This effect manifests itself as the mixing of fragments of the nuclear wave packet traveling back and forth.

D. The first turning point time t_R and the maximum nuclear dispersion time t_M

Here we pay attention to a few important time scales that are characteristic of the dynamics within the first oscillation period of each isotope and as a function of their reduced mass. We first investigate the arrival time of the wave packet at the first turning point t_R; this time corresponds to the time at which the bond length is minimum. One can clearly see from Fig. 8 that t_R scales as $\sqrt{\mu}$. This can be understood by modeling the PES of Fig. 1 with the Morse potential $V(R)=-D_e+D_e\{1-\exp[-\beta(R-R_e)]\}^2$, where D_e is the dissociation energy, R_e is the equilibrium internuclear distance, and β is the length scale [23]. With the harmonic approximation of this system, which reads

$$V(R)\approx -D_e+\beta^2 D_e X^2=-D_e+\tfrac{1}{2}\mu\omega^2X^2, \qquad (16)$$

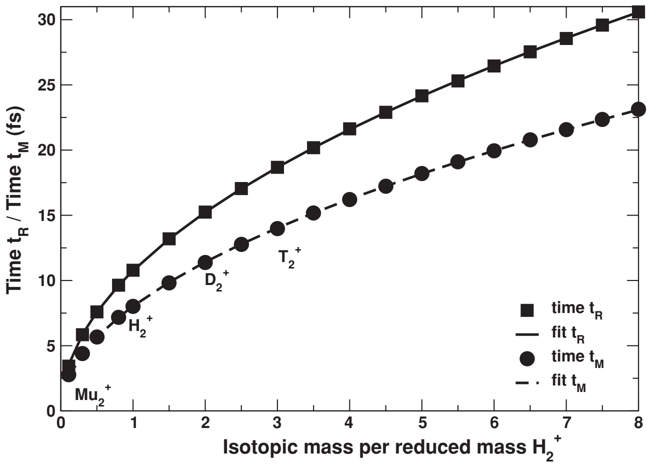

FIG. 8. Time at the first turning point t_R (squares), fit with $10.75\sqrt{\mu}$, and time t_M (circles) within the first oscillation period where the nuclear dispersion is maximum, fit with $8.0\sqrt{\mu}$, as a function of the reduced mass μ of different isotopes per the reduced mass of $H_2{}^+$, $\mu_{H_2{}^+}$.

where $X=R-R_e$, it turns out that the harmonic frequency is given by

$$\omega=\beta\sqrt{\frac{2D_e}{\mu}}. \qquad (17)$$

This implies that the oscillation period $T=2\pi/\omega$ scales as $\sqrt{\mu}$, which is in accordance with our numerical result.

Then the time t_M at which the nuclear dispersion becomes maximal is another time scale of interest. We found that this maximum nuclear dispersion is reached around R_e, i.e., within the first oscillation period at $t_M\approx 1.3t_R$, thus leading to $\sqrt{\mu}$ scale, as depicted in Fig. 8. This result can be understood as a consequence of quantum interference since it is precisely the time at which the mixing of fragments of the wave packet traveling back and forth reaches its maximum. Note that in our system, which is nonlinear (Morse oscillator), the number of eigenstates is finite and our wave packet contains a limited number of such eigenstates. In a harmonic oscillator (HO) case, however, the situation may be different under certain conditions. Indeed, it has been shown that in the HO case with infinite number of eigenstates, the wave packet keeps its shape throughout the propagation [24] and the nuclear dispersion is time independent. In all nonlinear systems the nuclear dispersion is time dependent even if the wave packet contains all eigenstates.

E. The autocorrelation

The wave packet dynamics in our systems lead us to explore not only their spreading and collapsing but also their revivals. We use the autocorrelation function $C(t)$, which contains the information about the revivals. $C(t)$ is defined as the overlap between the initial wave function with the time-evolved wave packet:

$$C(t)=\langle\Psi(r,z,R;0)|\Psi(r,z,R;t)\rangle. \qquad (18)$$

Figure 9 shows the autocorrelation function $C(t)$ for four selected isotopes. The oscillations observed throughout

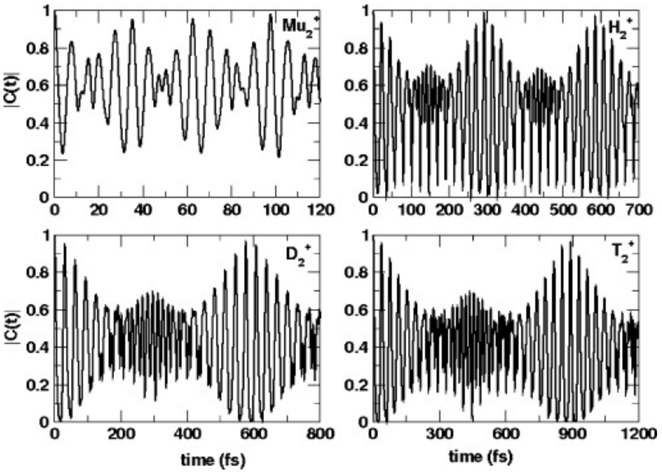

FIG. 9. Absolute value of the autocorrelation function $|C(t)|$ of different isotopes as a function of time. The revival time $t_{\rm rev}$ rapidly increases with the reduced mass μ and is approximated with $t_{\rm rev} = 300\mu/\mu_{H_2^+}$, where $\mu_{H_2^+}$ is the reduced mass of $H_2{}^+$.

demonstrate the wave packet spreading, collapsing, and reviving. This numerical experiment shows that the revival time $t_{\rm rev}$ linearly increases with the reduced mass μ and is specifically given by $t_{\rm rev} = 300\mu/\mu_{H_2^+}$, where $\mu_{H_2^+}$ is the reduced mass of $H_2{}^+$. As demonstrated below, this revival time can be predicted, assuming that our wave packet is an eigenstate of the Morse potential with the eigenenergy $E_n = \hbar(n + 1/2) - [\hbar^2\omega^2/(4D_e)](n + 1/2)^2$, where n is the principal quantum number. In this case $t_{\rm rev}$ is given by [25]

$$t_{\rm rev} = \frac{2\pi\hbar}{\frac{1}{2}\left|\frac{\partial^2 E_n}{\partial n^2}\right|} = \frac{4\pi}{\hbar\beta^2}\mu \propto \mu \tag{19}$$

since the length scale $\beta = \omega\sqrt{\mu/(2D_e)}$ is constant. Compared with all other considered observables, the revival time has the strongest dependence on the reduced mass. Therefore, the isotope effect is strongly pronounced for the revival time.

IV. CONCLUSION

We have demonstrated that a small change in a vibrating molecular mass can significantly alter the coupled electronic and nuclear fluxes monitored through an observer surface. As our test bed, we have considered the isotopes of the hydrogen molecular ions $H_2{}^+$ as well as some fictitious ones to allow for a large range of the mass variation from $Mu_2{}^+$ through $H_2{}^+$, $D_2{}^+$, $T_2{}^+$, until an isotope eight times heavier than $H_2{}^+$ was reached. In this mass range, both electronic and nuclear fluxes undergo large variations. To get better insights into the detailed physical phenomena in this system, several observables as well as time scales have been analyzed. These include the starting nuclear flux time t_S, the time delay $\Delta\tau$ that the nuclei takes to follow the electron when the electron first changes its direction (counterintuitive directionality issue), the electronic dispersions $(\Delta r, \Delta z)$ and the nuclear dispersion ΔR, the mean bond length $\langle R\rangle$, the maximum nuclear dispersion $(\Delta R)_{\rm max}$, the minimum nuclear bond $\langle R\rangle_{\rm min}$, and the revival time $t_{\rm rev}$. It turns out that each of the above-mentioned observables or time scales behaves monotonically with the reduced mass of the isotope. Scaling laws with respect to the reduced mass have been determined. Based on the Morse oscillator model, we have been able to confirm that the time at the first turning point t_R is proportional to $\sqrt{\mu}$ and that the revival period of each isotope scales linearly with μ, as clearly observed in our numerical experiments. It is also worth noticing that the overall dispersion is larger for light isotopes than heavy ones. This phenomenon is due to the quantun interference, predominantly developed by the nuclear wavepacket.

In view of the high sensitivity of the coupled electronic and nuclear flux and related observables with respect to a small molecular mass change, one can anticipate that these results will undoubtedly be of great importance not only for larger-scale molecules but also for experimental purposes.

ACKNOWLEDGMENTS

We are very grateful to Prof. C. Lasser (Zentrum Mathematik, Technische Universität München), Prof. J. Manz (Freie Universität Berlin), and Prof. H.-Ch. Hege (Zuse Institut Berlin) for very helpful and stimulating discussions. The financial support by Freie Universität Berlin via the Center for Scientific Simulation (CSS), by the DFG research center MATHEON, and by Deutsche Forschungsgemeinschaft, Projects Sfb 450 TPC1 is gratefully acknowledged.

---

[1] I. Barth, H.-C. Hege, H. Ikeda, A. Kenfack, M. Koppitz, J. Manz, F. Marquardt, and G. K. Paramonov, Chem. Phys. Lett. **481**, 118 (2009).

[2] A. Kenfack, F. Marquardt, G. K. Paramonov, I. Barth, C. Lasser, and B. Paulus, Phys. Rev. A **81**, 052502 (2010).

[3] M. Okuyama and K. Takatsuka, Chem. Phys. Lett. **476**, 109 (2009).

[4] M. Born and R. Oppenheimer, Ann. der Physik **84**, 457 (1927).

[5] S. Chelkowski, T. Zuo, O. Atabek, and A. D. Bandrauk, Phys. Rev. A **52**, 2977 (1995); G. K. Paramonov, Chem. Phys. Lett. **411**, 350 (2005).

[6] M. J. Jamieson and B. Zygelman, Phys. Rev. A **64**, 032703 (2001).

[7] E. Bodo, F. A. Gianturco, N. Balakrishman, and A. Dalgarno, J. Phys. B **37**, 3641 (2004).

[8] T. Stoecklin and A. Voronin, Phys. Rev. A **72**, 042714 (2005).

[9] J. Fedor, O. May, and M. Allan, Phys. Rev. A **78**, 032701 (2008).

[10] S. T. Chourou and A. E. Orel, Phys. Rev. A **80**, 034701 (2009).

[11] J. L. Nolte, B. H. Yang, P. C. Stancil, T.-G. Lee, N. Balakrishnan, R. C. Forrey, and A. Dalgarno, Phys. Rev. A **81**, 014701 (2010).

[12] O. Vendrell, F. Gatti, and H.-D. Meyer, J. Chem. Phys. **131**, 034308 (2009).

[13] D. K. Sasmal, S. Dey, D. K. Das, and K. Bhattachayaryya, J. Chem. Phys. **131**, 044509 (2009).

[14] A. D. Bandrauk, S. Chelkowski, and H. Lu, J. Phys. B **42**, 075602 (2009).

[15] G. K. Paramonov, Chem. Phys. Lett. **411**, 350 (2005).

[16] S. Chelkowski, T. Zuo, O. Atabek, and A. D. Bandrauk, Phys. Rev. A **52**, 2977 (1995).

[17] M. J. Frisch *et al.*, GAUSSIAN03, Revision C.02 (Gaussian, Inc., Wallingford, CT, 2004).

[18] T. H. Dunning, J. Chem. Phys. **90**, 1007 (1989).

[19] M. D. Feit, J. A. Fleck, and A. Steiger, J. Comp. Phys. **47**, 412 (1982).

[20] C. Lubich, *Zurich Lectures in Advanced Mathematics* (European Mathematical Society, Zurich, 2008).

[21] A. Vibok and G. G. Balint-Kurti, J. Phys. Chem. **96**, 8712 (1992).

[22] D. Stalling, M. Westerhoff, and H.-C. Hege, in *The Visualization Handbook*, edited by C. D. Hansen and C. R. Johnson (Elsevier, Amsterdam, 2005), Chap. 38, pp. 749–767.

[23] A. Kenfack and J. M. Rost, J. Chem. Phys. **123**, 204322 (2005).

[24] E. Schrödinger, Naturwissenschaften **14**, 664 (1926); I. R. Senitzky, Phys. Rev. **95**, 1115 (1954); S. T. Epstein, Am. J. Phys. **27**, 291 (1959).

[25] R. Bluhm, V. A. Kostelecky, and J. A. Porter, Am. J. Phys. **64**, 944 (1996).